Study of the Multi-Critical Parameters Characterizing the Instability Behavior of Translational Rockslides Considering the Excavation

ShenHai Liu , Liang Yang * , Mengyao Wang , Ming Shen , Yifan Sheng

Posted Date: 9 January 2024

doi: 10.20944/preprints202401.0748.v1

Keywords: translational rockslides; instability behavior; instability length; movement distance; excavation

Article

Study of the Multi-Critical Parameters Characterizing the Instability Behavior of Translational Rockslides Considering the Excavation

ShenHai Liu [1,2], Liang Yang [3,*], Mengyao Wang [3], Ming Shen [4] and Yifan Sheng [5]

[1] Institute of Advanced Studies, China University of Geosciences, WuHan 430074, China; ShenHai Liu: 18314406203@163.com;
[2] School of Jewelry, West YunNan University of Applied Sciences, YunNan 679100, China
[3] Faculty of Engineering, China University of Geosciences, WuHan 430074, China; wangmengyao507@126.com
[4] YunNan Zhicheng Water conservancy and hydropower Engineering Co., LTD, YunNan, China; Ming Shen: 13658843620@163.com
[5] Institute of Geological Survey, China University of Geosciences, Wuhan 430074, China; Yifan Sheng: yifansheng@cug.edu.cn
* Correspondence: Yangl507@cug.edu.cn

Abstract: Translational rockslides caused by toe excavation are one of the commonly seen geohazards in mountainous regions due to line traffic construction. Quantifying their failure extension length (FEL) and travel distance are of significant interest as well as huge challenges in landslide hazard assessment. In this paper, a simple criterion is proposed for predicting these two factors based on the principles of rigid body limit equilibrium and kinetic energy theorem. Further, the proposed criterion is validated against the field observations and numerical results with a practical case of the Xinjianan landslide, a medium-sized translational rockslide that occurred in 2013 in Nanchuan District, Chongqing. The findings indicate that a tiny discrepancy can be found in FEL between the field observations and the proposed criteria, while this discrepancy could be considerable in travel distance between different methods. However, the relative discrepancies all fall within 20%, deemed acceptable.

Keywords: translational rockslides; instability behavior; instability length; movement distance; excavation

1. Introduction

With the rapid economic development in China, infrastructure, industrial and civil buildings, as well as highway construction projects have been developing and extending to mountainous regions [1,2]. Owing to the control requirements of the line layout, excavation of some geological materials can sometimes be inevitable. However, these activities may cause deformations of original stable geological structures and further lead to their instability, posing great threats to highway construction and nearby buildings [3–5]. Consequently, to effectively reduce the risk of this type of slope failure, there is an urgent need to analyze their instability behavior. Overall, the instability behavior of landslides is a complex phenomenon influenced by various factors, such as geological structure, hydrogeology, and climate et al [6–8]. Given the abstract nature of landslide instability behavior, characterizing the risk of a landslide with realistic parameters provides a better tool to understand them, where the most significant parameters of failure extension length (FEL) and travel distance of the landslides are analyzed in this study.

Among various human engineering activities, slope excavation engineering is one of the most commonly seen activities triggering landslides [9–11]. The slope excavation-induced landslides are usually characterized by translational movement, where the rock slopes are prone to slides along the

 doi:10.20944/preprints202401.0748.v1

bedding planes of underlying strata aligned in a subparallel manner to topography [12–15]. Typical examples include the devastating White Deer sliding of 2011 [16], and the large horizontal bedding slide in Shanyang, Shaanxi in 2015 [17]. Hence, comprehensive research on the unstable behavior of such landslides is crucial for ensuring the safety and well-being of communities living in landslide-prone areas.

FEL, as a key parameter of engineering slope prevention design, can describe the instability behavior inside the slope [18–20]. Feng et al [25] and Deng et al [26] developed some theoretical formulas to calculate the FEL using a multi-layer slope model with the limit equilibrium method [21–24]. However, their formula includes several parameters that are hard to define in field applications. Furthermore, their models fail to determine the travel distance, which is another essential parameter in describing the behavior of slope instability. Hence, this paper aims to propose a simple model for determining the FEL in a single rock layer and obtaining the travel distance following slope instability.

Predicting the travel distance of a landslide is an exceedingly intricate problem, which is influenced by multiple aspects such as material properties, terrain conditions, the trajectory of movement, etc [27]. Thus far, there are three approaches to evaluating the travel distance of landslides: empirical models [28–30], theoretical models [30–32], and numerical simulation models [33–35]. Empirical models are the most popular which are based on the regression analysis between the travel distance and different geometric factors (e.g. difference in altitude, slope angle, and landslide volume, etc.) [36], while flow parameters or mechanical parameters of motion are not involved. Hence, it is a practical predictive means and many researchers have adopted this approach [37,38]. Notably, a reliable empirical model requires an adequate number of landslide samples. Regrettably, in actual excavation projects, engineers mainly focus on the steadiness, range of influence, or support methods of a stratified rock landslide, while paying minimal attention to its travel distance after instability, leading to a small number of such landslide samples. The final prediction model obtained from a limited number of sample data often has low precision and limited extensibility.

As computer technology has seen rapid advancement in the 21st century, it is now possible to predict the distance of landslide motion via numerical simulation [39–41]. Nonetheless, parameter selection in numerical simulation is a challenging endeavor, as some parameters require extensive testing, resulting in a considerable amount of time being spent [42], while theoretical models are able to evade the aforementioned issues to a certain extent, owing to the limited number of mechanical parameters involved. Consequently, numerical simulation is often used to confirm the accuracy of the results of theoretical models. Currently, the theoretical prediction models for landslide movement distance predominantly focus on high-speed and long-run-out landslides [43,44] and translational landslides [45]. These models fail to account for the influence of excavation factors and are unsuitable for application to such landslides. Moreover, although Yang et al [46] considered the effect of excavation on the movement distance of the translational landslides, the slide weight, a key parameter used to calculate the travel distance, was obtained by assigned, rather than derived from FEL, which will amplify the error in the results.

Considering the above-mentioned gaps, after analyzing the evolution process of this type of landslide, the paper proposed the theoretical model of multi-critical parameters including instability length and movement distance to describe the instability behavior of translational rockslides and validated its feasibility through examples and numerical simulation. The findings of this paper provide useful guidance for the prevention and prediction of these kinds of slope failures.

2. Methodology

The computation of the FEL stems from the rigid body limit equilibrium theory. Besides, the vertical accumulation range of the landslide movement is typically much larger than the horizontal range for translational rockslides, thus the movement distance is mainly deduced through the kinetic theorem and energy conservation principles.

Preprints (www.preprints.org) | NOT PEER-REVIEWED | Posted: 9 January 2024 doi:10.20944/preprints202401.0748.v1

Based on the field investigation, the FEL and actual displacement distance of the XinJiaNan landslide after instability was determined and then compared with the theoretical value to verify the feasibility of the theoretical model.

Dynamic modeling analysis was conducted using UDEC (Itasca Consulting Group, 2004) [47,48] to thoroughly inspect the effects of excavation on slope behavior. Calculations were performed to consider the two factors of rainfall and excavation in order to assess their impacts on the slope. Thereby, two types of boundary conditions are assigned to the model: excavation and excavation accompanied by hydrostatic pressure, and the kinematic evolution of the landslide was studied, validating the feasibility of the theoretical model.

3. Instability behavior

3.1. Evolution process

Without the influence of external forces, slopes tend to be steady over the long-term geological evolution process (Figure 1a). When road construction or open-pit mining is carried out, the stresses located around the slope are released, allowing them to readjust to the new state of balance, resulting in tension fractures around the rear margin (Figure 1b). As the project continues and rainfall occurs, the rear margin fractures expand, forming a tension crack, while surface water flows into the fractures, creating fracture water pressure and infiltration forces that cause the fractures to continue to expand in depth (Figure 1c). With the passage of time, after the fractures have expanded and connected, the overall landslide sliding force is greater than the resisting force, leading to the instability of the entire slope (Figure 1d) [49].

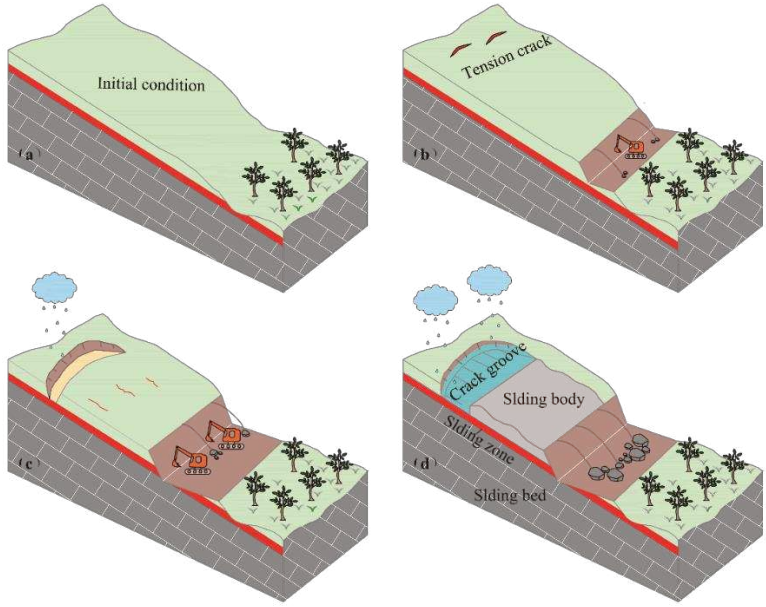

Figure 1. Evolution process of bedding rockslide under excavation unloading.

3.2. Mechanical analysis

Using the rigid body limit equilibrium method to derive the length of slope instability, the energy conservation theorem is employed to calculate the distance of slope movement.

3.2.1. Instability length

The excavation usually leads to local instability of the slope at the foot of the leading edge and tension cracks created at the trailing edge, which the state can be seen as understable at this time. Besides, the instability length calculated in this paper refers to the distance from the farthest crack at the trailing edge to the top of the excavated slope at the leading edge. A calculation model for

Preprints (www.preprints.org) | NOT PEER-REVIEWED | Posted: 9 January 2024 doi:10.20944/preprints202401.0748.v1

instability length is developed based on a typical bedding rock slope (Figure 2a). By the limit equilibrium theory of rigid bodies:

$$K=\frac{R}{T}=\frac{W_0\cos\partial\tan\varphi_0+c_0 l_{df}+\sigma l_{af}}{W_0\sin\partial} \tag{1}$$

Where K denotes the stability coefficient, W_0 stands for the weight of the sliding mass per unit width and ∂ represents the inclination angle of the rock stratum. l_{df} and l_{af} indicates the length of df and af, while c_0 and φ_0 denote the cohesion and internal friction angle respectively. σ represents the equivalent tensile strength perpendicular to the af. W_0 can be obtained from the following equation:

$$W_0=S_T\gamma=\left(S_{cde}+S_{abf}+S_{bcef}\right)\gamma \tag{(2)}$$

Where S_T represents the cross-sectional area of the sliding mass, and S_{cde}, S_{abf}, and S_{bcef} are the areas of triangular *cde*, *abf*, and rectangular *bcef*, respectively. γ are the weight of the sliding body. Besides, assuming l_{ef}=L, establish the side length relationship 3 to 5 from the geometric relationship:

$$l_{cd}=\frac{h}{\sin\beta},l_{ce}=l_{cd}\sin\left(\beta-\partial\right)=\frac{h\sin\left(\beta-\partial\right)}{\sin\beta} \tag{3}$$

$$l_{de}=l_{cd}\cos\left(\beta-\partial\right)=\frac{h\cos\left(\beta-\partial\right)}{\sin\beta},l_{ab}=\frac{l_{bf}}{\tan\left(\theta-\partial\right)}=\frac{h\sin\left(\beta-\partial\right)}{\sin\beta\tan\left(\theta-\partial\right)} \tag{4}$$

$$l_{af}=\frac{h\sin\left(\beta-\partial\right)}{\sin\beta\cos\left(\theta-\partial\right)\tan\left(\theta-\partial\right)},L_0=l_{df}=l_{de}+l_{ef}=\frac{h\cos\left(\beta-\partial\right)}{\sin\beta}+L \tag{5}$$

From equations 3-5, obtain the S_{cde}, S_{abf}, and S_{bcef}:

$$S_{cde}=\frac{l_{de}\times l_{ce}}{2}=\frac{h^2\sin\left(\beta-\partial\right)\cos\left(\beta-\partial\right)}{2\sin^2\beta} \tag{6}$$

$$S_{abf}=\frac{l_{ab}\times l_{bf}}{2}=\frac{h^2\sin^2\left(\beta-\partial\right)}{2\sin^2\beta\tan\left(\theta-\partial\right)} \tag{7}$$

$$S_{bcef}=l_{ef}\times l_{bf}=\frac{Lh\sin\left(\beta-\partial\right)}{\sin\beta} \tag{8}$$

Substituting equations 6-8 into 2 yields:

$$W_0=\frac{\left[h^2\sin\left(\beta-\partial\right)\cos\left(\beta-\partial\right)\tan\left(\theta-\partial\right)+h^2\sin^2\left(\beta-\partial\right)+2Lh\sin\beta\sin\left(\beta-\partial\right)\tan\left(\theta-\partial\right)\right]\gamma}{2\sin^2\beta\tan\left(\theta-\partial\right)} \tag{9}$$

substituting equations 9 into 1, and the following can be derived:

$$L\left(\frac{\gamma h\sin\left(\beta-\partial\right)\left(K\sin\partial-\cos\partial\tan\varphi_0\right)}{\sin\beta}-c_0\right)=\frac{c_0 h\cos\left(\beta-\partial\right)}{\sin\beta}+\frac{\sigma h\sin\left(\beta-\partial\right)}{\sin\beta\cos\left(\theta-\partial\right)\tan\left(\theta-\partial\right)}-\frac{\gamma\left[h^2\sin\left(\beta-\partial\right)\cos\left(\beta-\partial\right)\tan\left(\theta-\partial\right)+h^2\sin^2\left(\beta-\partial\right)\right]\left(K\sin\partial-\cos\partial\tan\varphi_0\right)}{2\sin^2\beta\tan\left(\theta-\partial\right)} \tag{10}$$

$$Command\quad A=\frac{\gamma h\sin\left(\beta-\partial\right)\left(K\sin\partial-\cos\partial\tan\varphi_0\right)}{\sin\beta} \tag{11}$$

Preprints (www.preprints.org) | NOT PEER-REVIEWED | Posted: 9 January 2024 doi:10.20944/preprints202401.0748.v1

$$B = \frac{c_0 h \cos(\beta - \partial)}{\sin \beta} \tag{12}$$

$$D = \frac{\sigma h \sin(\beta - \partial)}{\sin \beta \cos(\theta - \partial) \tan(\theta - \partial)} \tag{13}$$

$$M = \frac{\gamma \left[h^2 \sin(\beta - \partial) \cos(\beta - \partial) \tan(\theta - \partial) + h^2 \sin^2(\beta - \partial) \right] (K \sin \partial - \cos \partial \tan \varphi_0)}{2 \sin^2 \beta \tan(\theta - \partial)} \tag{14}$$

Substituting equations 11 through 14 into 10 results in:

$$L = \frac{B + D - M}{A - c_0} \tag{15}$$

Getting the final instability length l_{ac}:

$$l_{ac} = L + l_{ab} = \frac{B + D - M}{A - c_0} + \frac{h \sin(\beta - \partial)}{\sin \beta \tan(\theta - \partial)} \tag{16}$$

Where β is the slope excavation angle, θ represents the angle between the trailing edge crack and the horizontal plane. Additionally, h refers to the excavation height of the sliding mass.

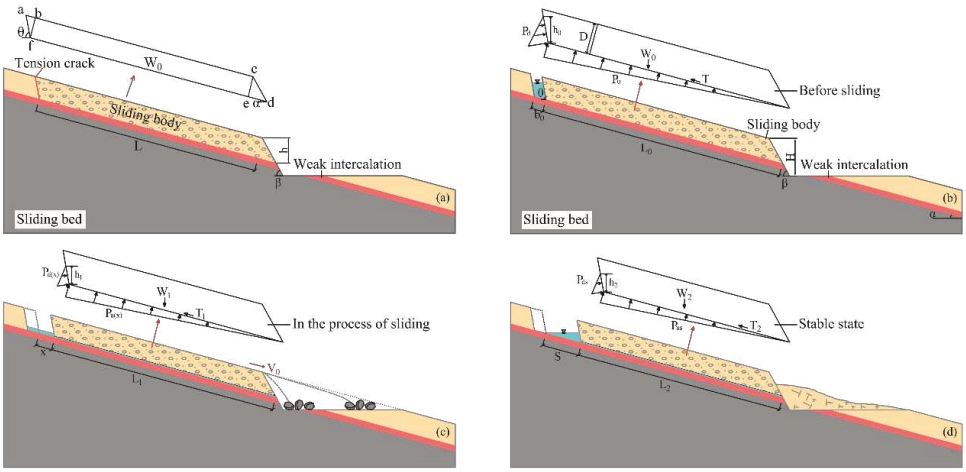

Figure 2. Mechanical computational model for describing instability behavior: (a) combined (b) before instability, (c) moving, (d) the balance of slope in the end.

3.2.2. Runout distance

The calculation model for slope instability to stability, divided into three stages (I~III), is illustrated in Figure 2b-2d. The water head heights of the trailing edge fractures in stages II and III are represented by h1 and h_2 respectively, while the lengths of the bottom surface of the sliding mass along the sliding direction in the latter two stages are denoted by L_1 and L_2. W_1 and W_2 refer to the unit width weight of the slope in the aforementioned stages, and b0 represents the length of the fracture along the sliding surface prior to slope instability. H stands for the excavation height, x denotes the distance traveled by the sliding mass on the slope, and d is the average thickness of the sliding body. V_0 represents the speed at which the sliding mass moves at distance x, while G denotes the moving distance of the sliding body on the slope in stage III.

During intense rainfall conditions, a considerable amount of rainwater infiltrates the tension cracks at the trailing edge, creating hydrostatic pressure. Furthermore, water infiltration induces uplift pressure along the sliding surface. During landslide motion, four forces should be considered: self-gravity W_1, anti-sliding force f_1, hydrostatic pressure P_d (x), and uplift pressure P_u (x).

Preprints (www.preprints.org) | NOT PEER-REVIEWED | Posted: 9 January 2024 doi:10.20944/preprints202401.0748.v1

Additionally, the sliding mass decreases continually during the movement owing to the formation of a free face resulting from front edge excavation, and result in these forces undergo constant changes during stage II, which is distinct from the scenario where the impact of excavation factors is not taken into account.

Assuming that the volume of water in the cracks at the rear edge of the landslide remains constant, and θ is nearly vertical. The water-filled cross-sectional areas s0 and s1 in the cracks during the I and II stages can be expressed by Equations 17 and 18, respectively:

$$s_0 = \frac{b_0 \sin(\theta-\partial)(2h_0 - b_0\cos(\theta-\partial))}{2} \tag{17}$$

$$s_1 = h_1(b_0+x)\sin(\theta-\partial) \tag{18}$$

When $s_0=s_1$, the relationship between h_0 and h_1 and the motion distance x can be expressed as follows:

$$h_1 = \frac{b_0(2h_0 - b_0\cos(\theta-\partial))}{b_0+x} \tag{19}$$

Set $N=b_0(2h_0 - b_0\cos(\theta-\partial))$, So $h_1=N/(b_0+x)$.

The relationship between W_0, W_1, and x can be expressed:

$$W_1 = \frac{W_0(L_0-x)}{L_0} \tag{20}$$

The relationships among L_0, L_1, and L_2 are established through the following equations：

$$\begin{aligned} L_1 &= L_0 - x \\ L_2 &= L_0 - G \end{aligned} \tag{21}$$

In the II stage, Equation 22 depicts the hydrostatic pressure $P_{d(x)}$ and the uplift pressure $P_{u(x)}$. The hydrostatic pressure $P_{d(x)}$ can be divided into two forces, namely a parallel force $P_{d1(x)}$ and a perpendicular force $P_{d2(x)}$, as illustrated in Equation 23. Additionally, the anti-sliding force f_1 is as shown in Equation 24:

$$P_{d(x)} = \frac{\gamma_w h_1^2}{2}, P_{u(x)} = \frac{\gamma_w h_1(L_0-x)}{2} \tag{22}$$

$$P_{d1(x)} = \frac{\gamma_w h_1^2 \sin(\theta-\partial)}{2}, P_{d2(x)} = \frac{\gamma_w h_1^2 \cos(\theta-\partial)}{2} \tag{23}$$

$$f_1 = \left(W_1\cos\partial - \frac{\gamma_w h_1(L_0-x)}{2} - \frac{\gamma_w h_1^2\cos(\theta-\partial)}{2}\right)\tan\varphi_0 + c_o L_1 \tag{24}$$

The shear strength parameter of the sliding belt in Equation 24 should be the residual strength parameter.

Assuming that the sliding mass comes to a halt at a distance of G on the slope. The kinetic energy of the landslide when it moves a distance x (0<x<G) is determined by two parts: the gravitational potential energy required to overcome resistance and the hydrostatic pressure that performs work. Therefore, the law of energy conservation can be applied to derive the following equation:

$$\frac{m_1 v_0^2}{2} = W_G - W_{f1} + W_{pd(x)} \tag{25}$$

Preprints (www.preprints.org) | NOT PEER-REVIEWED | Posted: 9 January 2024 doi:10.20944/preprints202401.0748.v1

In Equation 26-29, m1 represents the mass of the sliding body at a given moving distance x. WG denotes the work that is accomplished by the gravity of the sliding mass during this movement. Additionally, W_{f1} represents the work that is done by the anti-sliding force, while $W_{pd(x)}$ refers to the work that is accomplished by the hydrostatic pressure at the trailing edge. The details are as follows:

$$m_1 = W_1 / g \tag{26}$$

$$W_G = \int_0^x W_1 \sin\partial dx \tag{27}$$

$$W_{f1} = \int_0^x f_1 dx \tag{28}$$

$$W_{pd(x)} == \int_0^x P_{d1(x)} dx \tag{29}$$

Where g represents the acceleration of gravity, by substituting Equation 20 into 27, we can obtain W_G:

$$W_G = W_0 x \sin\partial - \frac{W_0 x^2 \sin\partial}{2L_0} \tag{30}$$

By substituting Equations 20, 23, and 24 into 28 and 29, we obtain the following expressions for W_{f1} and $W_{pd(x)}$:

$$W_{f1} = W_0 \cos\partial \tan\varphi_0 \left(x - \frac{x^2}{2L_0} \right) + \left(\gamma_w N \tan\varphi_0 \left[x - (b_0 + L_0) In \left(\frac{b_0 + x}{b_0} \right) \right] \right) / 2 \tag{31}$$
$$+ \frac{\gamma_w N^2 \tan\varphi_0 \cos(\theta - \partial)}{2(b_0 + x)} - \frac{\gamma_w N^2 \tan\varphi_0 \cos(\theta - \partial)}{2b_0} + c_0 L_0 x - \frac{c_0 x^2}{2}$$

$$W_{pd(x)} = \frac{\gamma_w K^2 \sin(\theta - \partial)}{2b_0} - \frac{\gamma_w K^2 \sin(\theta - \partial)}{2(b_0 + x)} \tag{32}$$

Substituting Equations 30 to 32 into 25 yields:

$$\frac{m_1 v_0^2}{2} = W_0 x \sin\partial - \frac{W_0 x^2 \sin\partial}{2L_0} - \left(\gamma_w N \tan\varphi_0 \left[x - (b_0 + L_0) In \left(\frac{b_0 + x}{b_0} \right) \right] \right) / 2 \tag{33}$$
$$- W_0 \cos\partial \tan\varphi_0 \left(x - \frac{x^2}{2L_0} \right) - c_0 L_0 x + \frac{c_0 x^2}{2} + \frac{\gamma_w N^2 \left(\sin(\theta - \partial) + \tan\varphi_0 \cos(\theta - \partial) \right)}{2b_0}$$
$$- \frac{\gamma_w N^2 \left(\sin(\theta - \partial) + \tan\varphi_0 \cos(\theta - \partial) \right)}{2(b_0 + x)}$$

Order $I = \sin(\theta - \partial) + \tan\varphi_0 \cos(\theta - \partial)$, and V_0 can be expressed:

Preprints (www.preprints.org) | NOT PEER-REVIEWED | Posted: 9 January 2024 doi:10.20944/preprints202401.0748.v1

$$v_0=\left\{\frac{2gL_0x\sin\partial-g\cos\partial\tan\varphi_0\left(2L_0x-x^2\right)-gx^2\sin\partial}{L_0-x}+\frac{gL_0c_0\left(x^2-2L_0x\right)}{W_0\left(L_0-x\right)}-\frac{\gamma_w gL_0N\tan\varphi_0\left[x-\left(b_0+L_0\right)In\left(\frac{b_0+x}{b_0}\right)\right]}{W_0\left(L_0-x\right)}+\frac{\gamma_w gN^2L_0I}{W_0b_0\left(L_0-x\right)}-\frac{\gamma_w gN^2L_0I}{W_0\left(L_0-x\right)\left(b_0+x\right)}\right\}^{\frac{1}{2}} \tag{34}$$

When the moving distance reach G, in accordance with the principle of energy conservation:

$$W_{f1}=W_G+W_{pd(x)} \tag{35}$$

Substitute x=G into Equation 35 to obtain:

$$\begin{aligned}&W_0\cos\partial\tan\varphi_0\left(G-\frac{G^2}{2L_0}\right)+\left(\gamma_wN\tan\varphi_0\left[G-\left(b_0+L_0\right)In\left(\frac{b_0+G}{b_0}\right)\right]\right)/2\\&+\frac{\gamma_wN^2\tan\varphi_0\cos\left(\theta-\partial\right)}{2\left(b_0+G\right)}-\frac{\gamma_wN^2\tan\varphi_0\cos\left(\theta-\partial\right)}{2b_0}+c_0L_0G-\frac{c_0G^2}{2}\\&=W_0G\sin\partial-\frac{W_0G^2\sin\partial}{2L_0}+\frac{\gamma_wN^2\sin\left(\theta-\partial\right)}{2b_0}-\frac{\gamma_wN^2\sin\left(\theta-\partial\right)}{2\left(b_0+G\right)}\end{aligned} \tag{36}$$

G can be calculated using Equation 36, with relevant parameters derived from real scenarios. The total displacement of a landslide comprises three components. Firstly, the horizontal distance X_0 covered by the slider during its initial movement in the air. Secondly, the horizontal displacement X_1+... X_n of the sliding body as it collides with the ground repeatedly (assuming n collisions) until its normal velocity reaches 0. Lastly, there is the displacement X_{n+1} generated by the block sliding on the ground, as depicted in Figure 3.

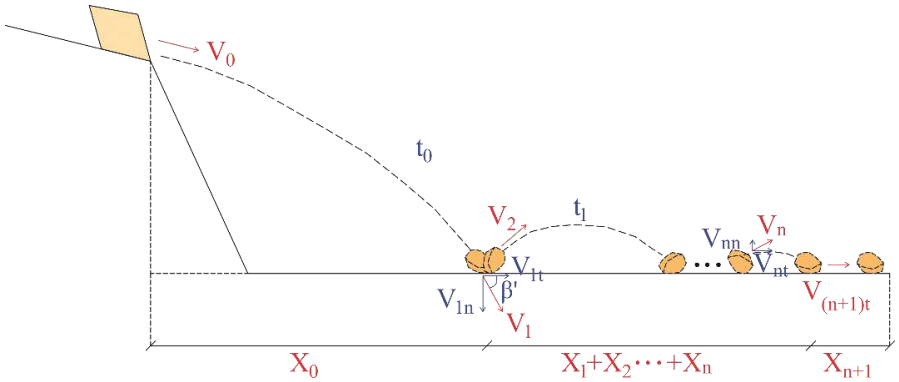

Figure 3. Runout process of sliding body.

Command Y=$H-\frac{d}{2\sin\left(\theta-\partial\right)}$, we can obtain:

$$V_0\sin\left(\partial\right)t_0+\frac{gt_0^2}{2}=Y,\ X_0=V_0\cos\left(\partial\right)t_0,\ \frac{m_1V_1^2}{2}=\frac{m_1V_0^2}{2}+m_1gY \tag{37}$$

T_0, X_0, and V_1 can be expressed as:

$$t_0=\frac{\left(V_0^2\sin^2\partial+2gY\right)^{\frac{1}{2}}-V_0\sin\partial}{g}$$

Preprints (www.preprints.org) | NOT PEER-REVIEWED | Posted: 9 January 2024 doi:10.20944/preprints202401.0748.v1

$$X_0=\frac{V_0\cos\partial\left[\left(V_0^2\sin^2\partial+2gY\right)^{\frac{1}{2}}-V_0\sin\partial\right]}{g},V_1=\sqrt{V_0^2+2gY} \tag{38}$$

When a block collides with the ground at a velocity of V_1, the incomplete elastic collision results in a loss of energy and a decrease in the block's velocity. To describe this phenomenon, we introduce the normal restitution coefficient R1n and the tangential restitution coefficient R1t. The relationship between the initial normal velocity V_{1n} and tangential velocity V_{1t} of the block prior to the collision, and the resulting normal velocity V_{2n} and tangential velocity V_{2t} of the block after the collision can be expressed as follows:

$$V_{2n}=V_{1n}R_{1n},V_{2t}=V_{1t}R_{1t} \tag{39}$$

V_{1n} and V_{1t} can be expressed:

$$V_{1n}=V_1\sin\beta',\quad V_{1t}=V_1\cos\beta' \tag{40}$$
$$\tan\beta=\frac{V_0\sin\partial+gt_0}{V_0\cos\partial},\quad \beta=\arctan\left(\frac{V_0\sin\partial+gt_0}{V_0\cos\partial}\right)$$

Where β' is the angle between V_1 and the horizontal plane (Figure 3):

X_1 represents the movement distance of the block between the first collision and the second collision, which can be expressed as following:

$$X_1=V_{2t}t_1,\quad t_1=\frac{2V_{2n}}{g} \tag{41}$$

Further, X_1 can be described as:

$$X_1=\frac{2R_{1n}R_{1t}V_{1n}V_{1t}}{g} \tag{42}$$

Similarly, X_2 … X_n can be expressed as:

$$X_2=\frac{2R_{1n}^2R_{1t}^2V_{1n}V_{1t}}{g},\ldots X_n=\frac{2R_{1n}^nR_{1t}^nV_{1n}V_{1t}}{g} \tag{43}$$

The second part of the movement distance can be calculated as following:

$$X_1+X_2+\ldots+X_n=\frac{2R_{1n}R_{1t}V_{1n}V_{1t}}{g}+\frac{2R_{1n}^2R_{1t}^2V_{1n}V_{1t}}{g}+\ldots+\frac{2R_{1n}^nR_{1t}^nV_{1n}V_{1t}}{g} \tag{44}$$
$$=\frac{2V_{1n}V_{1t}R_{1n}R_{1t}\left[1-\left(R_{1n}^nR_{1t}^n\right)\right]}{g\left(1-R_{1n}R_{1t}\right)}$$

At the n+1 collision, the normal velocity of the block attenuates to 0, and the block slides on the ground at a velocity of $V_{(n+1)t}$, and the associated motion equation can obtain:

$$V_{(n+1)t}=V_{1t}R_{1t}^n,\frac{m_1V_{(n+1)t}^2}{2}=\mu m_1gX_{n+1} \tag{45}$$

The third stage movement distance X_{n+1} can be expressed as:

$$X_{n+1}=\frac{V_{(n+1)t}^2}{2\mu g}=\frac{V_{1t}^2R_{1t}^{2n}}{2\mu g} \tag{46}$$

The final runout distance X_t of the landslide can be gained as follows:

Preprints (www.preprints.org) | NOT PEER-REVIEWED | Posted: 9 January 2024 doi:10.20944/preprints202401.0748.v1

$$X_t = \frac{V_0 \cos\partial\left[\sqrt{V_0^2 \sin^2\partial + 2gY} - V_0 \sin\partial\right]}{g} + \frac{2V_{1n}V_{1t}R_{1n}R_{1t}\left[1-\left(R_{1n}^n R_{1t}^n\right)\right]}{g\left(1-R_{1n}R_{1t}\right)} + \frac{V_{1t}^2 R_{1t}^{2n}}{2\mu g} \tag{47}$$

Substituting Equation 38 and 40 into 47 yields:

$$X_t = \frac{V_0 \cos\partial\left[\sqrt{V_0^2 \sin^2\partial + 2gY} - V_0 \sin\partial\right]}{g} + \frac{2\left(V_0^2+2gY\right)s\text{in}\,\beta'\cos\beta' R_{1n}R_{1t}\left[1-\left(R_{1n}^n R_{1t}^n\right)\right]}{g\left(1-R_{1n}R_{1t}\right)} + \frac{\left(V_0^2+2gY\right)\cos\beta' R_{1t}^{2n}}{2\mu g} \tag{48}$$

Generally speaking, the velocity of landslide will undergoes an initial increase until reach maximum followed by a subsequent decrease. The maximum speed occurs when the anti sliding force equals the sliding force once again, and can be expressed:

$$f_1 = P_{dl(x)} + W_1 \sin\partial \tag{49}$$

49 can be written as:

$$\left(W_1 \cos\partial - \frac{\gamma_w h_1\left(L_0 - x\right)}{2} - \frac{\gamma_w h_1^2 \cos\left(\theta-\partial\right)}{2}\right)\tan\varphi_0 + c_o L_1 = \frac{\gamma_w h_1^2 \sin\left(\theta-\partial\right)}{2} + W_1 \sin\partial \tag{50}$$

Eventually available：

$$\frac{W_0\left(L_0-G_0\right)\left(\cos\partial\tan\varphi_0 - \sin\partial\right)}{L_0} - \frac{\gamma_w N\tan\varphi_0\left(L_0-G_0\right)}{2\left(b_0+G_0\right)} + c_o\left(L_0-G_0\right) = \frac{\gamma_w N^2\left(\cos\left(\theta-\partial\right)\tan\varphi_0 + \sin\left(\theta-\partial\right)\right)}{2\left(b_0+G_0\right)^2} \tag{51}$$

Where G_0 represent the movement distance of the sliding mass on the slope when the block speed reaches the maximum, which can be obtained by substituting the relevant parameters into Equation 51, and Vmax of the sliding mass on the slope can be obtained as follows:

$$v_{\max} = \left\{\begin{array}{l} \dfrac{2gL_0G_0\sin\partial - g\cos\partial\tan\varphi_0\left(2L_0G_0 - G_0^2\right) - gG_0^2\sin\partial}{L_0-G_0} + \\ \dfrac{gL_0c_0\left(G_0^2 - 2L_0G_0\right)}{W_0\left(L_0-G_0\right)} - \dfrac{\gamma_w gL_0N\tan\varphi_0\left[G_0 - \left(b_0+L_0\right)In\left(\dfrac{b_0+G_0}{b_0}\right)\right]}{W_0\left(L_0-G_0\right)} \\ + \dfrac{\gamma_w gN^2L_0N}{W_0b_0\left(L_0-G_0\right)} - \dfrac{\gamma_w gN^2L_0I}{W_0\left(L_0-G_0\right)\left(b_0+S_0\right)} \end{array}\right\}^{\frac{1}{2}} \tag{52}$$

Moreover, given the monotonically increasing correlation between X_t and V, the ultimate displacement distance X_t of the landslide can be formulated as follows:

Preprints (www.preprints.org) | NOT PEER-REVIEWED | Posted: 9 January 2024 doi:10.20944/preprints202401.0748.v1

$$X_t = \frac{V_{max}\cos\partial\left[\sqrt{V_{max}^2\sin^2\partial+2gY}-V_{max}\sin\partial\right]}{g}+ \frac{2\left(V_{max}^2+2gY\right)s\,in\,\beta'\cos\beta' R_{ln}R_{lt}\left[1-\left(R_{ln}^n R_{lt}^n\right)\right]}{g\left(1-R_{ln}R_{lt}\right)}+\frac{\left(V_{max}^2+2gY\right)\cos\beta' R_{lt}^{2n}}{2\mu g} \quad (53)$$

4. Case verification

Taking Xinjianan landslide as an example, the feasibility of the model is verified through case analysis and numerical simulation.

The landslide is located in Dongcheng Office, Nanchuan District, Chongqing. At 8:00 pm on December 27, 2012, a bedding slide with a volume of approximately 24.06 × 10^4 m^3 occurred on the slope. The landslide exhibits a longitudinal extent of approximately 304 m, an average width of roughly 106 m, and a thickness ranging from 2.5 to 30.0 m. Its primary sliding direction is approximately 30 ° (Figures 4a, 4b). The sliding mass primarily comprises cataclastic rock mass, with limestone and shale composing the lithology. Besides, the slip zone is a weak interlayer containing shale, while the sliding bed is composed of limestone from the Feixianguan Formation of the Triassic System, with a rock occurrence of 30 °∠ 26 °. The leading edge of the landslide underwent excavation as a result of open-pit mining, reaching a height range of 9.2 to 42.6 m (Figure 4e). Specifically, the front edge of the 1-1 'to 3-3' profile was excavated at varying heights of 28 m, 42.6 m, and 21.7 m, respectively (Figure 5). Prior to the onset of slope instability, tensile cracks measuring between 0.5 and 2.5 meters in width were observed along the rear edge (Figure 4c), northeast front edge, and middle of the west boundary. Following the instability event, the tensile fracture groove widened, with the rock mass structure appearing to be most intact along section 3-3' (Figure 4d), followed by section 2-2', while section 1-1' exhibited the most pronounced fracturing (Figure 4f).

4.1. Case analysis

Utilizing the outcomes of on-site investigations, survey reports, and records documented by on-site patrol personnel, the calculation parameters for each section were obtained. The strength paramaters of the sliding zone soil was determined through indoor direct shear tests, with c_0, φ_0 at 13.5 kN/m^2, 9.5° respectively. Considering that the excavation platform serves as a road following its construction, reference was made to the findings of Zhang et al. [50] (Table 1) to ascertain that R_{1n} and R_{1t} are 0.4 and 0.87, respectively. Following seven collisions, the normal velocity was only 0.16% of the speed before the initial collision, can take for its impact negligible. The number of collisions, n, was set at 7. The sliding friction coefficient was determined as 0.58, based on the results of Huang et al. [51], and the numerical values of other parameters are presented in Table 1.

Table 1. Calculation parameters of each section of Xinjianan landslide.

Profile	γ (kN/m^3)	ɵ (°)	β (°)	h(m)	b_0 (m)	h_0 (m)	L_0 (m)	W_0 (kN/m)	H (m)
1-1′	21.5	82	74	19.4	1.5	5.5	196.0	62975.50	28.0
2-2′	21.5	82	69	34.7	1.2	5.5	216.0	114972.54	42.6
3-3′	21.5	82	76	19.1	2.2	3.5	30.0	9323.86	21.7

Preprints (www.preprints.org) | NOT PEER-REVIEWED | Posted: 9 January 2024 doi:10.20944/preprints202401.0748.v1

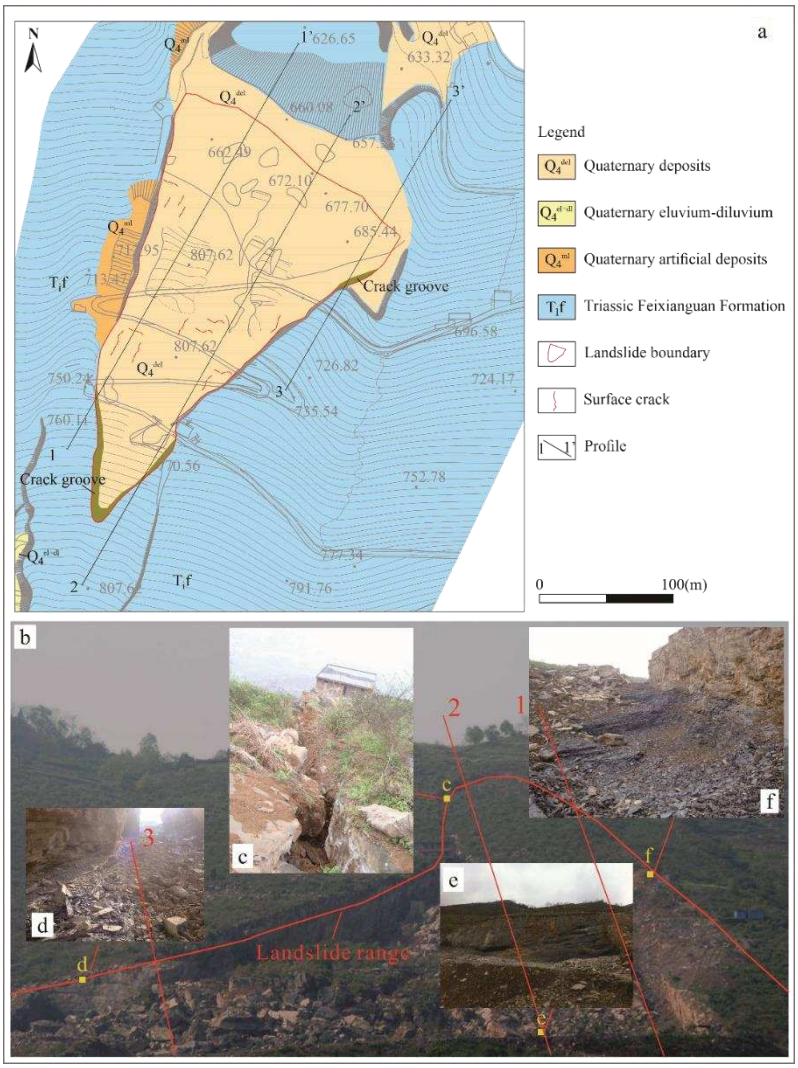

Figure 4. Overview and basic characteristics of landslide.

Substituting the above parameters into Eqs. 18, 54 and 55 gives the results of the FEL and movement distance. The outcome were then compared with the real results (Table 2).

Table 2. Comparison between theoretical calculated and actual of landslide.

Profile	l_{ac} (m)	l_{ac}' (m)	X_t (m)	X_t' (m)	absolute error	relative error
1-1′	170.5	187.2	75.22	69.5	16.7/5.72	8.9%/8.23%
2-2′	175.2	197.7	82.5	72.4	22.5/1.83	11.38%/13.95%
3-3′	20.8	25.7	27.14	25.7	4.0/0.15	19.07%/5.6%

Where l_{ac} and $l_{ac'}$ represent the FEL derived from theoretical calculations and on-site measurements, while X_t and $X_{t'}$ denote the displacement distances obtained from calculations and surveys.

Based on the findings, it is evident that the FEL obtained from the calculation is smaller than the actual, whereas the moving distance from computing is larger. Nevertheless, the error is within 20%, which is deemed acceptable, proving that these methods possess some degree of practical applicability.

Preprints (www.preprints.org) | NOT PEER-REVIEWED | Posted: 9 January 2024 doi:10.20944/preprints202401.0748.v1

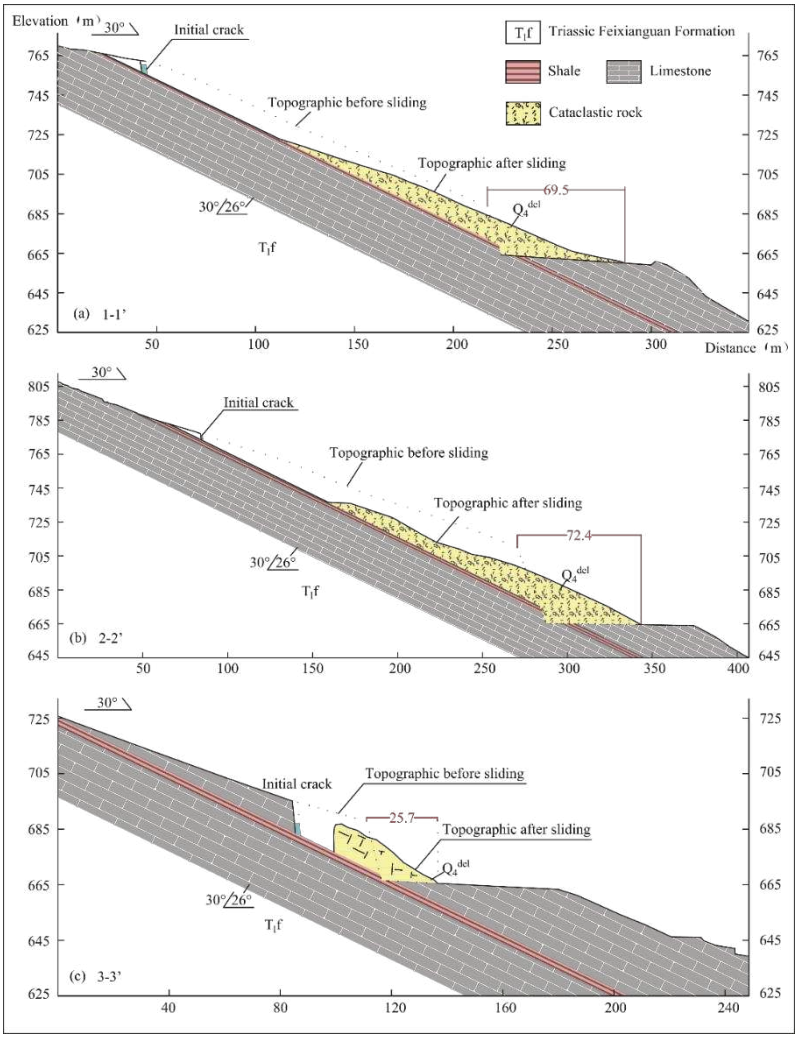

Figure 5. Engineering geological profile. a, b and c represent 1-1′, 2-2′ and 3-3′ respectively.

Table 2. Comparison between theoretical calculated and actual of landslide.

Profile	l_{ac} (m)	l_{ac}' (m)	X_t (m)	X_t' (m)	absolute error	relative error
1-1′	170.5	187.2	75.22	69.5	16.7/5.72	8.9%/8.23%
2-2′	175.2	197.7	82.5	72.4	22.5/1.83	11.38%/13.95%
3-3′	20.8	25.7	27.14	25.7	4.0/0.15	19.07%/5.6%

4.2. Numerical simulation analysis

Two types of environmental scenarios were therefore considered: 1) excavation, 2) excavation + hydrostatic pressure.

4.2.1. Model implementation and parameter determination

A two-dimensional model (Figure 6) is developed considering a vertical cross-section (Profile 1 in Figure 4a) oriented SW-NE that is perpendicular to the topographic surface. This cross-section extends from the slope crest (770 m) to the slope base (659 m). The slide material, as stated above in Section 4.1, is composed mainly of rubble, represented by blocks in the model, and silty clay, which is treated as the joint between these rock blocks that bonds them together (Figure 4a). Field investigations revealed that the slope base is dominated by layered bedrocks. The model is constrained by displacement-type boundary conditions: no bottom vertical displacement and no

Preprints (www.preprints.org) | NOT PEER-REVIEWED | Posted: 9 January 2024 doi:10.20944/preprints202401.0748.v1

horizontal displacement at the left side are permitted. In this case, rigid blocks are assumed whereas the joints are assumed to behave according to an elastoplastic law with the Mohr-Coulomb failure criterion. Besides, since the sliding mass consists of cataclastic rock, which shape is inherently uncertain, and can be delineated using Voronoi.

To accurately reconstruct the damage behavior using inversion, the primary parameters and boundary conditions are established as follows:

1. The strength parameters of both the slip zone and slip body are initially set to their peak strength until tension cracks emerge at the trailing edge. Subsequently, the strength parameters of the slip zone and slip body are set to their residual strength.

2. Once tension cracks appear at the trailing edge of the slip body, hydrostatic pressure is applied along the rupture surface of both the trailing edge and substrate.

The materia properties of landslide are shown in Table 3, and the mechanical characteristics of the matrix and joints properties assigned to the joint network are listed in Table 4. These parameters were initially acquired from in indoor experiments and relevant literature [52–54]. Afterward, via inverse analysis until appropriate parameters are obtained to predict the possible kinematic evolution of the landslide in different cases.

Table 3. The materia properties of landslide.

Stage	Position	γ (kN/m³)	B (Pa)	S (Pa)	c (kPa)	φ (°)	T(Mpa)
Excavation	1	21.5	7.2×10^{9}	5.5×10^{9}	26.3	24.4	1.5
	2	19.5	3.8×10^{8}	2.1×10^{8}	19.5	21.5	0.35
	3	25.5	8.9×10^{11}	6.9×10^{11}	95	50	120
Hydrostatic pressure	1	20.6	2.1×10^{9}	1.5×10^{9}	20.6	13.8	0.8
	2	18.6	8.6×10^{7}	7.6×10^{7}	13.5	9.5	0.2
	3	24.8	8.9×10^{11}	6.9×10^{11}	95	50	120

1~3 represent the sliding body, zone, and bed respectively. B: bulk modulus, S: shear modulus, T: tensile strength.

Table 4. Properties of rock matrix and joints.

Stage	Position	Jk_n (GPa/m)	Jk_s (GPa/m)	Jc (kpa)	Jt (Mpa)	*Jf* (°)
Excavation	1	12.0	4.0	24.5	0.8	23.2
Hydrostatic pressure	1	10.0	2.5	19.8	0.4	12.5

Jk_n/Jk_s: joint normal/shear stiffness; Jc: joint cohesion; Jt: joint tensile strength; *Jf*: joint friction.

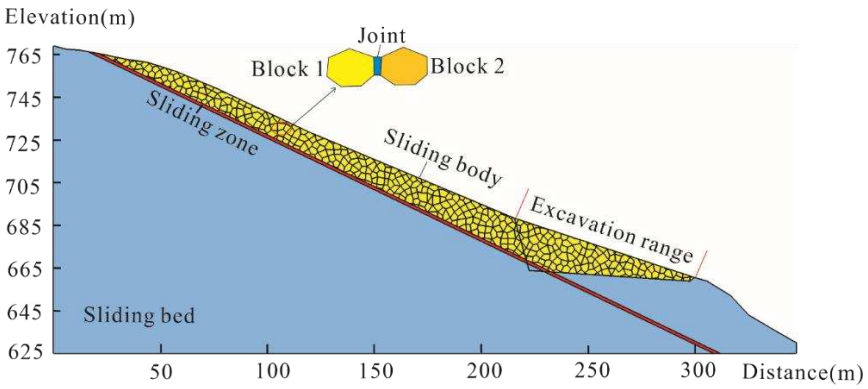

Figure 6. Schematic slope geometry used in the numerical study.

4.2.2. Result of numerical tests

Preprints (www.preprints.org) | NOT PEER-REVIEWED | Posted: 9 January 2024 doi:10.20944/preprints202401.0748.v1

Considering the excavation conditions alone, partial slope damage occurs primarily at the front edge, resulting in block stones rolling off up to a distance of approximately 18m (Figure 7a). Besides, tension cracks appear at the rear edge, with the maximum distance of approximately 182 m from the front edge (Figure 7b). However, because of cracks at the trailing edge, once encounter continuous rainfall, will lead to a rapid decrease in the strength parameters of the sliding mass and sliding zone. In this scenario, hydraulic conditions and parameter weakening should be considered. Therefore, hydrostatic pressure was applied along the trailing edge cracks and weak layers of the landslide then, and the parameters were set as residual strength parameters. The final results are shown in Figures 7c and 7d. The outcome is an overall slope failure with a maximum movement distance of approximately 66.5m (Figure 7c, 7d), which is in good agreement with the theoretical model conclusion.

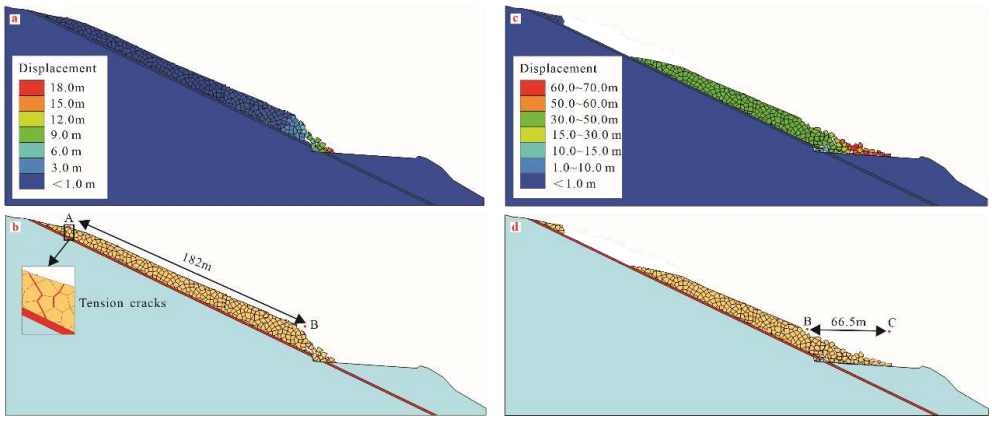

Figure 7. Slope deformation under the influence of excavation and hydrostatic pressure. (a, b) slope deformation under excavation conditions, (c, d) slope deformation combined excavation and hydrostatic pressure.

5. Discussion

The theoretical framework presented in this paper primarily pertains to sliding-tensile translational rockslides belongs to overall destruction, typically characterized by inclination angles ranging from 20 to 30°. However, given the variability of landslide parameters and intricate internal dynamics, it is inadvisable to rely solely on this model for determining instability length and movement distance during slope design. Instead, integrating the theoretical calculations with numerical simulations can yield more robust outcomes.

6. Conclusion

The paper presents an analysis of the instability behavior of translational rockslide under excavation conditions, focusing on two critical parameters: slope instability length and post-damage movement distance. A theoretical model for these parameters is proposed based on the principles of limit equilibrium of rigid bodies and conservation of momentum. The feasibility of this model is demonstrated through example verification and numerical simulations.

Under excavation conditions, the translational rock slope typically induces localized damage at the leading edge and tension cracks at the trailing edge. Subsequent rainfall is the primary factor contributing to the overall damage of these slopes, which is consistent with the findings of numerical simulations.

The theoretical model presented in this paper exhibits certain discrepancies with the actual system, which is mainly attributed to the uncertainties in strength parameters and the deviations in geometric parameter estimations. Specifically, the calculated instability length is smaller than the actual value, while the movement distance is larger. Therefore, it is recommended to integrate the theoretical model with numerical simulations to determine these two critical parameters in slope engineering design and risk assessment.

Data Availability Statement: Not applicable.

Acknowledgments: This work is supported by the National Natural Science Foundation of China (Nos. 42077277), and Youth Science Foundation (Nos. 42107160).

References

1. Wu, Lili, et al. "Research on the excavation stability evaluation method of Chaqishan ancient landslide in China." Engineering Failure Analysis 141 (2022): 106664. https://doi.org/10.1016/j.engfailanal.2022.106664
2. Y. Togashi, K. Mizuo, M. Osada, T. Yamabe, et al., Evaluating Changes in the Degree of Saturation in Excavation Disturbed Zones Using a Stochastic Differential Equation, Computers and Geotechnics. 143 (2022), https://doi.org/10.1016/J.COMPGEO.2021.104598.
3. T. Liu, Y. Xie, Z.H. Feng, Y.B. Luo, et al., Better Understanding the Failure Modes of Tunnels Excavated in the Boulder-Cobble Mixed Strata by Distinct Element Method, Engineering Failure Analysis. 116 (104712) (2020) 1–14. https://doi:10.1016/j.engfailanal.2020.104712.
4. S.S. Xu, H. Lei, C. Li, H.Q. Liu, et al., Model Test on Mechanical Characteristics of Shallow Tunnel Excavation Failure in Gully Topography, Engineering Failure Analysis. 119 (2021), 104978 (Prepublish), https://doi:10.1016/j.engfailanal.2020.104978.
5. B. Bayer, A. Simoni, D. Schmidt, L. Bertello, Using Advanced InSAR Techniques to Monitor Landslide Deformations Induced by Tunneling in the Northern Apennines Italy, Engineering Geology. 226 (2017) 20–32, https://doi.org/10.1016/j.enggeo.2017.03.026.
6. Guo, Changbao, et al. "Study of an ancient landslide reactivation mechanism based on centrifuge model testing: an example of the Jiangdingya ancient landslide reactivation in 2018, Gansu Province, China." Landslides 20.1 (2023): 127-141. https://doi.org/10.1007/s10346-022-01978-5
7. Zhang, Chonglei, et al. "Large-scale shaking table test on seismic behaviour of anti-slide pile-reinforced bridge foundation and gravel landslide: a case study." Bulletin of Engineering Geology and the Environment 80 (2021): 1303-1316. https://doi.org/10.1007/s10064-020-02006-3
8. Guo, Jian, et al. "The effect of topography on landslide kinematics: a case study of the Jichang town landslide in Guizhou, China." Landslides 17 (2020): 959-973. https://doi.org/10.1007/s10346-019-01339-9
9. E. Botero, E. Ovando, M.J. Mendoza, Successful prediction of slope failure in an excavation trial, Engineering Failure Analysis. 109 (C) (2020) 104392, https://doi.org/10.1016/j.engfailanal.2020.104392.
10. K.R. Praveen, J. Chophel, J. Wangchuk, K. Tshewang, et al., IBIS-FM Radar as A Tool for Monitoring Hill Slopes During Excavations in Hydropower Projects: A Case Study from Bhutan Himalayas, Energy Geoscience. 1–7 (2021), https://doi.org/10.1016/J.ENGEOS.2021.11.001.
11. F. Florin, L. Maria, D. Ciprian, A. IzabelaMaria, Investigations on the Stability of the Right Slope in the Area of Anina Wastewater Treatment Plant, Revista Minelor / Mining Revue. 27 (4) (2022) 7–18, https://doi.org/-10.2478/MINRV-2021-0030.
12. Du J, Shi X, Chai B, et al. Force and energy equilibrium-based analytical method for progressive failure analysis of translational rockslides: formulation and comparative study. Landslides, 20(2): 475-488, (2023). https://doi.-org/10.1007/s10346-022-01980-x
13. Wang W, Song H, Zhang Z, et al. Landslide Multi-attitude Data Measurement of Bedding Rock Slope Model[J]. International Journal of Parallel Programming, 48 (2020): 928-939. https://doi.org/10.1007/s10766-019-00638-x
14. Peng Y, Dong S, Lu Z, et al. A method for calculating permanent displacement of seismic-induced bedding rock landslide considering the deterioration of the structural plane. Frontiers in Earth Science, (2023): 2272. https://doi.org/10.3389/feart.2022.1026310
15. Dai Z, Zhang L, Wang Y, et al. Deformation and failure response characteristics and stability analysis of bedding rock slope after underground adverse slope mining. Bulletin of Engineering Geology and the Environment, 80.6 (2021): 4405-4422. https://doi.org/10.1007/s10064-021-02258-7
16. Yu, X., Gong, B. & Tang, C. Study of the slope deformation characteristics and landslide mechanisms under alternating excavation and rainfall disturbance. Bull Eng Geol Environ 80 (2021), 7171–7191. DOI: https://doi.org/10.1007/s10064-021-02371-7
17. Wang J Y, Li L, Zheng D G, et a1. Characteristics of Apparent Dip Slide and Movement Process of the "8.12" Shanyang Rockslide. Journal of Catastrophology, 33,1 (2018): 111~ 116. (in Chinese with English abstract) DOI: https://doi.org/10. 3969/j.issn.1000-811 X.2018.01.020
18. Zhu X, Xie L, Tang Y, et al. Progressive Formation of Retrogressive Landslide and the Lateral Length of Instability. Applied Sciences, 13.2 (2023): 799. https://doi.org/10.3390/app13020799
19. Li J, Chen S, Yu F, et al. Reinforcement mechanism and optimisation of reinforcement approach of a high and steep slope using prestressed anchor cables. Applied Sciences, 10.1 (2019): 266. https://doi.org/10.33-

90/app10010266
20. Liu Z, Qiu H, Ma S, et al. Surface displacement and topographic change analysis of the Changhe landslide on September 14, 2019, China. Landslides, 18 (2021): 1471-1483. https://doi.org/10.1007/s10346-021-01626-4
21. Johari A, Mousavi S. An analytical probabilistic analysis of slopes based on limit equilibrium methods. Bulletin of Engineering Geology and the Environment, 78 (2019): 4333-4347. https://doi.org/10.1007/s10064-018-1408-1
22. Cheng H, Zhou X. A novel displacement-based rigorous limit equilibrium method for three-dimensional landslide stability analysis. Can Geotech J 52 (2015):2055–2066. https://doi.org/10.1139/cgj-2015-0050
23. Zhou XP, Cheng H. Analysis of stability of three-dimensional slopes using the rigorous limit equilibrium method. Eng Geol 160 (2013):21–33. https://doi.org/10.1016/j.enggeo.2013.03.027
24. Sengani F, Allopi D. Accuracy of Two-Dimensional Limit Equilibrium Methods in Predicting Stability of Homogenous Road-Cut Slopes. Sustainability, 14.7 (2022): 3872. https://doi.org/10.3390/su14073872
25. Feng J, Zhou D P, Jiang N,Yang T. (2007). On the Extent of Bedding Slipping Rockmass of Consequent Rock Slope. Journal of Mountain Science, 03:376-380. (In Chinese with English abstract)
26. Deng R G, Zhou D P, Li A H, et al. (2002). On the Critical Length of Unstable Rock Stratum on bedrock slope. Chinese Journal of Geotechnical Engineering, 24.2:178-181. (in Chinese with English abstract)
27. Su X, Wei W, Ye W, et al. Predicting landslide sliding distance based on energy dissipation and mass point kinematics. Natural Hazards, 96 (2019): 1367-1385. https://doi.org/10.1007/s11069-019-03618-z
28. Hattanji T, Moriwaki H. Morphometric analysis of relic landslides using detailed landslide distribution maps: implications for forecasting travel distance of future landslides. Geomorphology 103 (2009): 447–454. https://doi.org/10.1016/j.geomorph.2008.07.009
29. Guo D P, Hamada M, He C, Wang Y F, Zou Y L. An empirical model for landslide travel distance prediction in Wenchuan earthquake area. Landslides 11.2 (2014):281–291. https://doi.org/10.1007/s10346-013-0444-y
30. Guo C B, Zhang Y S, Montgomery D R, et al. How unusual is the long-runout of the earthquake-triggered giant Luanshibao landslide, Tibetan Plateau, China? Geomorphology 259 (2016):145–154. https://doi.org/10.1016/-j.geomorph.2016.02.013
31. Hungr O. A model for the runout analysis of rapid flow slides, debris flows, and avalanches. Can Geotech J 32 (1995):610–623
32. Miao T D, Liu Z Y, Niu Y H, Ma C W. A sliding block model for the runout prediction of high-speed landslides. Can Geotech J 38.2 (2001):217-226. DOI: 10.1139/cgj-38-2-217
33. Wang J D, Xiao S F, Zhang Z Y. The mechanism for movement of irrigation-induced high-speed loess landslide. J Eng Geol 9.3 (2001):241–246 (In Chinese with English abstract)
34. He S M, Liu W, Wang J. Dynamic simulation of landslide based on thermo-poroelastic approach. Comput. Geosci. 75 (2015): 24–32. DOI: https://doi.org/10.10-16/j.cageo.2014.10.013
35. Scaringi G, Fan X, Xu Q, et al. Some considerations on the use of numerical methods to simulate past landslides and possible new failures: the case of the recent Xinmo landslide (Sichuan, China). Landslides, 15.7 (2018): 1359-1375. DOI: https://do-i.org/10.1007/s10346-018-0953-9
36. Huang Y, Li G, Xiong M. Stochastic assessment of slope failure run-out triggered by earthquake ground motion. Nat. Hazards 101 (2020): 87–102. DOI: https://d-oi.org/10.1007/s11069-020-03863-7.
37. Mitchell A, McDougall S, Nolde N, et al. Rock avalanche runout prediction using stochastic analysis of a regional dataset. Landslides 17 (2020): 777–792. https://doi.org/10.1007/s10346-019-01331-3
38. Zhang Z, Zeng R, Meng X, et al. Estimating landslide sliding distance based on an improved Heim sled model. Catena, 204 (2021): 105401. DOI: https://doi.org/10.10-16/j.catena.2021.105401
39. Jiang P, Chen J J. Displacement prediction of landslide based on generalized regression neural networks with K -fold cross-validation. Neurocoputing 198 (2016): 40-47. DOI: https://doi.org/10.1016/j.neucom.2015.08.118
40. Liu Y, Xu C, Huang B, et al. Landslide displacement prediction based on multi-source data fusion and sensitivity states. Engineering Geology. 271 (2020): 105608. DOI: https://doi.org/10.1016/j.enggeo.2020.105608
41. Li X, Tang X, Zhao S, et al. MPM evaluation of the dynamic runout process of the giant Daguangbao landslide. Landslides, 18.4 (2021): 1509-1518. DOI: https://doi.o-rg/10.1007/s10346-020-01569-2
42. Zhang C, Yin Y, Yan H, et al. Centrifuge modeling of multi-row stabilizing piles reinforced reservoir landslide with different row spacings. Landslides. 20.3 (2022): 559-577. https://doi.org/10.1007/s10346-022-01994-5
43. Zhou C, Cao Y, Yin K, et al. 2022. Characteristic comparison of seepage-driven and buoyancy-driven landslides in Three Gorges Reservoir area, China. Engineering Geology, 301: 106590. DOI: https://doi.org/10.1016/j.en-ggeo.2022.106590
44. Ge Y F, Tang H M, Li Wei, et al. (2016). Evaluation for Deposit Areas of Rock Avalanche Based on Features

of Rock Mass Structure. Earth Science, 41.9: 1583-1592. (In Chinese with English abstract)
45. Dai X R, Zhao J J, Lai Q Y, et al. (2022). Movement Process and Formation Mechanism of Rock Avalanche in Chada, Tibet Plateau. Earth Science. 47.6:1932-1944. (In Chinese with English abstract) DOI: https://doi.org/10.-3799/dqkx.2021.205
46. Tang R, Xu Q, Wu B, et al. (2017). Method of sliding distance calculation for translational landslides. Rock and Soil Mechanics. 39.03:1009-1019+1070. (In Chinese with English abstract)
47. Yang L,Wang Y, Zhang Q et al. A theoretical model about runout distance of bedding rock landslide under excavation uploading [J/OL]. Earth Science:1-15[2023-06-05]. http://kns.cnki.net/kcms/detail/42.1874.P.20230-420.1013.002.html. (In Chinese with English abstract)
48. Itasca, 2004. UDEC Version 4.0 Universal Distinct Element Code. Itasca Consulting Group, Inc.
49. Li X M,Yan E C,YanY, et al. (2019). Deformation Zoning and Treatment of a Toppling Deformation Slope Beside the Diversion Channel of a Hydropower Station. Bulletin of Geological Science and Technology.38 (3):227-235. (In Chinese with English abstract)
50. Mu C L. 2017. Study on deformation instability evolution mechanism and prediction during excavating process of bedded rock slope - A case of slope as the studied object in the Gasoline construction site. Doctoral dissertation. Chengdu University of Technology. (In Chinese with English abstract)
51. Zhang Y H, Zhang M X, Cheng Q. (2017). Kinematics analysis for calculating distance of rockfalls on typical loose media slope. Journal Of ShangHai University (Natural Science). 23.06: 949-960. (In Chinese with English abstract). DOI: https://doi.org/10.12066/j.issn.1007-2861.1806
52. Huang R Q, Liu W H. (2008). Study on the movement characteristics of rolling rock blocks on platform. Advances in Earth Science. 05: 517-523. (In Chinese with English abstract)
53. Huang D, Gu D M, Song Y X, et al. (2018). Towards a complete understanding of the triggering mechanism of a large reactivated landslide in the Three Gorges Reservoir. Engineering Geology, 238: 36-51. https://doi.org/10.-1016/j.enggeo.2018.03.008
54. Guglielmi Y, Cappa F, Binet S. (2005). Coupling between hydrogeology and deformation of mountainous rock slopes: Insights from La Clapière area (southern Alps, France). Comptes Rendus Geoscience, 337.13: 1154-1163. https://doi.org/10.1016/j.crte.2005.04.016